# Two Dimensional Imaging of the Virtual Source of a Supersonic Beam: Helium at 125 K

S. D. Eder,*,[†] G. Bracco,[‡,†] T. Kaltenbacher,[†] and B. Holst[†]

[†]Department of Physics and Technology, University of Bergen, Allégaten 55, 5007 Bergen, Norway
[‡]Department of Physics, University of Genova, CNR-IMEM, V Dodecaneso 33, 16146 Genova, Italy

ABSTRACT: Here we present the first two-dimensional images of the virtual source of a supersonic helium expansion. The images were obtained using a free-standing Fresnel zone plate with an outermost zone width of 50 nm as imaging lens and a beam cooled to around 125 K. The nozzle diameter was 10 μm. The virtual source diameter was found to increase with stagnation pressure from 140 ± 30 μm at $p_o = 21$ bar up to 270 ± 25 μm at $p_o = 101$ bar. The experimental results are compared to a theoretical model based on the solution of the Boltzmann equation by the method of moments. The quantum mechanical cross sections used in the model have been calculated for the Lennard-Jones (LJ) and the Hurly-Moldover (HM) potentials. By using a scaling of the perpendicular temperature that parametrizes the perpendicular velocity distribution based on a continuum expansion approach, the LJ potential shows a good overall agreement with the experiment. However, at higher pressures the data points lie in between the two theoretical curves and the slope of the trend is more similar to the HM curve. Real gas corrections to enthalpy are considered but they affect the results less than the experimental errors.
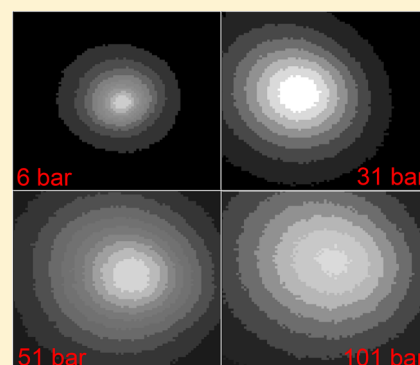
1. INTRODUCTION

Low (thermal) energy, neutral atom and molecule beams are important in several fields of science and applied research.[1−4] They are employed for example in high energy physics for jet target experiments,[5] in experiments on molecular interaction, in spectroscopic studies of fragile species,[6,7] and in the investigation of matter wave properties and quantum coherence.[8−12]

The quantum properties of helium allow the production of particularly intense beams with a very narrow velocity distribution. This has been exploited in the investigation of surface properties such as structures, vibrations, and adatom diffusion studies[13−18] of different crystalline materials including oxides,[19] inorganic[20] and organic layers,[21−23] organic crystals,[24] nanostructures,[25,26] as well as amorphous and disordered systems.[27,28] Another application is surface deposition experiments using seeded beams.[29−31] The unique properties of helium beams have also been exploited in speckle-diffraction experiments[32] and microscopy.[33−35]

In a supersonic expansion, also referred to as a free jet expansion,[2,36] gas at a stagnation pressure p_o and temperature T_o expands from a high pressure reservoir through a small nozzle into a low pressure ambient background chamber. The mean free path λ_o of the atoms or molecules in the reservoir must be small compared to the nozzle diameter d_N ($d_N \gg \lambda_o$). Such an expansion generates a high intensity beam with a very small velocity spread.[2] The beam can be characterized by the following two velocity distributions: The so-called parallel velocity distribution that can be measured in time-of-flight experiments along the beam axis and the perpendicular velocity

distribution that can be measured with additional intensity scans across the beam.

The parallel velocity distribution has been investigated in a wide range of works[2,3,36−39] because it is crucial for determining the energy resolution in inelastic scattering experiments, which has been a well-established technique for many years for measuring surface vibrations and adatom diffusion. The perpendicular velocity distribution on the other hand has not been investigated so intensely up till now. The first major investigations were performed by Beijerinck et al.[40−43] More recently new investigations have been performed by DePonte et al.[44] and Reisinger et al.[45,46]

Beijerinck et al. introduced the concept of the "virtual source" as a mean to describe the spacial distribution of a molecular beam. By tracing the straight trajectories of the expanding atoms in the molecular flow regime backward, one can find an "area of least confusion", close to the nozzle exit plane, where the atom trajectories pass through a minimum cross section. This minimum cross section area is referred to as the virtual source.[40] It is closely related to the perpendicular velocity distribution and thereby the lateral coherence of the beam (see Figure 1).

The lateral coherence (virtual source size) of the beam is a property that is crucial for a range of new developments in molecular beams, for example, microscopy and quantum coherence experiments. In standard helium scattering experi-
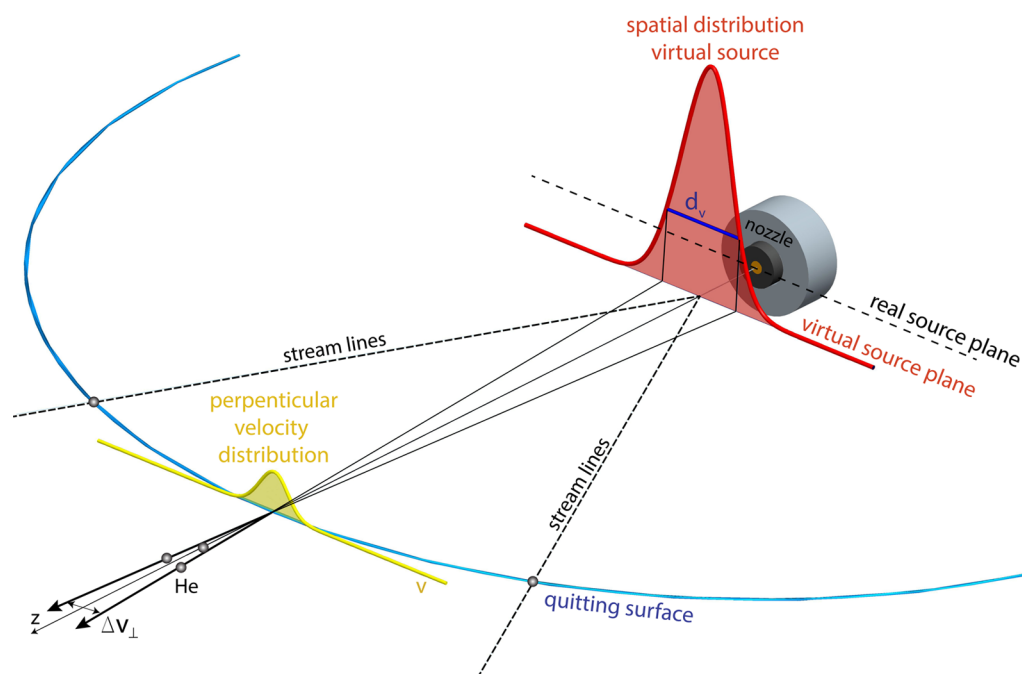
Figure 1. Diagram illustrating the virtual source concept. By tracing the straight trajectories of the expanding atoms in the molecular flow regime backward, one can find an area of least confusion, close to the nozzle exit plane, where the atom trajectories pass through a minimum cross section. The quitting surface represents the region where the atoms/molecules cease to collide and move into the molecular flow regime. In reality, this will be a blurred boundary. However, in the sudden freeze approach, applied in our theoretical model, it is treated as an abrupt transition.

ments, a large skimmer, typically 400 μm in diameter, is used in front of the nozzle to define the beam. This skimmer spans the entire virtual source for all pressures typically used. In microscopy on the other hand, the size of the focus is determined by a collimating microskimmer (typically 1 μm diameter or less) inserted in front of the nozzle instead of the large skimmer. Since the microskimmer is much smaller than the virtual source and the virtual source expands with increasing pressure, the flux through a microskimmer will not necessarily increase with pressure even though the flux through the nozzle does. Because sufficient intensity is a crucial issue for neutral helium microscopy, the beam flux through the microskimmer is a very important parameter to optimize.

In this paper, we investigate the virtual source size of neutral, supersonic helium beams. We present measurements of a cooled helium beam in a range of stagnation pressures from 6 to 101 bar. A particular aim of this work is to test the validity of a theoretical expansion model, which we have developed to predict the performance of beams for microscopy. The model is based on the solution of the Boltzmann equation and on applying quantum mechanical cross sections calculated for the Lennard-Jones (LJ) and the Hurly-Moldover (HM) potentials. The two potentials are analytical with the latter having a very simple expression and therefore it is used in a broad range of applications. HM has shown to be best suited to describe He beam properties at low temperatures while LJ fits better at high temperatures.[47] For the work presented here, the model has been further extended to take real gas properties of helium into account. We have previously used the model to describe helium beam measurements obtained close to room temperature (320 K).[45] When these first measurements were presented we did not have the option of cooling the beam and test the model in a different temperature regime. We find that the model is remarkably stable, describing also the new experimental data very well, despite a temperature span of almost 200 K. Apart

from testing our model experimentally in a new temperature regime, we present here the first 2D images of a supersonic molecular beam expansion.

2. THEORETICAL MODEL

Our theoretical model of a supersonic expansion has been described in previous articles[45,46] therefore we only give a brief summary here, pointing out the differences compared to previous calculations.

In the supersonic expansion through a nozzle of diameter d_N, the atomic collisions cause a decrease of the gas temperature and its random thermal energy in the source is converted into the beam translational kinetic energy. For high gas pressures p_o and short and converging nozzles, gas viscosity and energy loss due to heat exchange with the nozzle walls can be neglected and the gas expansion can be treated as an adiabatic and isentropic process.[36] The velocity distribution $f(\vec{v})$ narrows during the expansion until the collision frequency becomes negligible due to the density decrease, thus $f(\vec{v})$ cannot evolve further. The region separating the collisionless region from the part closer to the nozzle where collisions are present is called the quitting surface. From the source up to the quitting surface, the gas flow can be approximated as a continuum flow; beyond the quitting surface the gas is in a molecular flow regime (see Figure 1).

In the sudden freeze model, which assumes a sharp quitting surface, the evolution of $f(\vec{v})$ up to the transition into the molecular flow regime can be calculated by means of the Boltzmann equation (BE) solved by using an approximated method, the so-called method of moments that is discussed in ref 48. This method is based on the following assumptions: (i) the expansion is spherically symmetric, that is, all the streamlines diverge from a common point source, (ii) the flow properties depend only on the distance from the source,

and (iii) the velocity distribution can be approximated by an anisotropic velocity distribution which is the product of two Maxwellian functions, $f_M(v_\parallel)$ and $f_M(v_\perp)$ for the directions parallel or perpendicular to the diverging streamlines as discussed in the Introduction. The different widths of the two Maxwellian functions are often parametrized by two temperatures, $T_\parallel$ and $T_\perp$ respectively.

The BE was initially solved for the helium Lennard-Jones potential and later on the method was extended to other analytical helium two-body potentials[47,49] and recently also to diatomic molecules such as deuterium.[46] In the present work, we compare the results of the LJ (12-6) potential[50] and the HM potential.[51] The starting parameters for solving the BE are obtained from the stagnation conditions in the source, that is, the source temperature T_o and pressure p_o. In our previous articles,[45,46] the results were obtained treating helium as a perfect gas. In the present work, we performed the calculations for helium treated as a real gas as well, employing the equation of state obtained by McCarty.[52] We compare the results with the perfect gas case.

The distance D_{QS} of the quitting surface from the source is determined by a suitable value of the ratio of temperatures $\rho = T_\perp/T_\parallel$ which decreases during the expansion. As in previous works $\rho = 0.01$ has been chosen.

From the knowledge of D_{QS} and the perpendicular temperature at the quitting surface $T_\perp^*$, the width of the virtual source can be calculated in two different ways. In the first way, the results of the BE are used directly in the relationship derived by geometrical considerations[40,45]

$$d_B^{pot} = 2\sqrt{2\ln 2}\,\frac{D_{QS}\sqrt{\frac{k_B T_\perp^*}{m}}}{u} \tag{1}$$

where pot is LJ or HM depending on the potential, m is the He mass, and u is the most probable velocity of the gas (flow velocity). This estimation does not represent satisfactorily the data as shown in Section 4. In the second way, the estimation of the perpendicular temperature is calculated approximating the gas expansion by a continuum expansion in which the temperature scales with the distance r from the source as[2]

$$T_C(r) = 0.287 \cdot T_o r^{-4/3}$$

where T_o is the source temperature. Assuming the same distance for the quitting surface as in the first way, the final temperature at the quitting surface can be calculated as $T_C^* = T_C(D_{QS})$. The width of the virtual source can then be determined as in eq 1 with $T_\perp^*$ replaced by $T_C^* = T_C(D_{QS})$. This second evaluation provides much better agreement with the experiment as shown in Section 4.

3. EXPERIMENTAL SETUP

Figure 2 shows the experimental setup used to image the virtual source. The molecular beam apparatus in which the measurements were performed is popularly known as MaGIE. A detailed description can be found in ref 53. A neutral helium beam was created by a supersonic expansion from a high pressure reservoir (6−101 bar) through a 10 μm diameter nozzle into a high vacuum (10^{-5}−10^{-3} mbar). All experiments were carried out with a liquid nitrogen cooled nozzle source at a source temperature of nominally 125 K, corresponding to a velocity $v = 1140$ ms^{-1} and a wavelength λ of 0.0875 nm ($E \approx$ 27 meV). Because of a minor technical problem with the
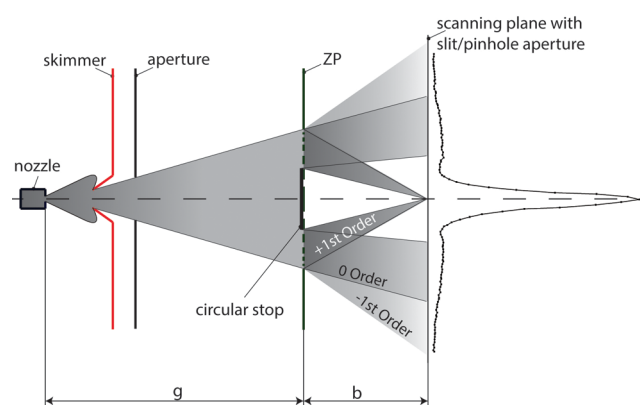
Figure 2. Experimental setup used for the measurements of the virtual source diameter. The helium beam passes through a 400 μm skimmer into the beamline. It is collimated by a 300 μm diameter aperture before it hits the ZP, mounted so that the virtual source is in the object plane. The ZP projects an image of the virtual source on to the image plane. The image is recorded by scanning with a slit or a pinhole aperture. The helium atoms passing the slit/pinhole aperture are detected in an electron bombardment detector. An image of the virtual source scan profile is shown on the right side of the figure. The circular stop eliminates the main part of the 0 order beam. The measured scan profile is a sum of the +1 order (the focus), 0 order, and −1 order contributions (higher order contributions can be ignored, since they contribute with less than 1.2% of the incident total intensity[56,57]).

source, the actual beam temperature (determined using time-of-flight (TOF)),[54] increased slightly with pressure from around 121 K at 10 bar to 126 K at 100 bar. The neutral helium atom beam passed from the source chamber through a 400 ± 50 μm diameter skimmer into the adjacent beamline consisting of several ultrahigh vacuum chambers. The beam was further collimated by a 300 ± 5 μm diameter pinhole aperture (National Aperture, Inc.) before it reached the focusing Fresnel zone plate (ZP). The Fresnel zone plate was positioned at a fixed distance to the virtual source $g = 1538 \pm 5$ mm. This defined the object plane distance. The distance between the zone plate and detector can be moved mechanically (see ref 35) so that the position of the image plane b could be determined experimentally. The theoretical position of the image plane is given by the first order focal length f of the ZP. f is determined by the wavelength λ of the incident beam, the radius of the ZP r_i, and the number of zones N (see ref 56). Our zone plate has $N = 2700$ and a diameter of 540 μm. Using $\lambda = 0.0875$ nm and $g = 1538 \pm 5$ mm results in an image plane position of $b = 387 \pm 2$ mm. Because of a technical problem it was not possible to move the image plane position further away than $b = 378 \pm 5$ mm with a resulting demagnification factor $M = 0.245 \pm 0.004$. All measurements were performed at this image plane position. Geometrical considerations show that the widening of the source diameter due to this shifted image plane position is negligible compared to the overall precision of the measurements. The width of the outermost zone in our ZP is 50 nm. A circular stop, 162 μm in diameter, blocks the central part of the ZP to minimize the influence of the zero order beam (see Figure 2). A detailed description on the fabrication process of the ZP can be found in ref 55.

We used two different types of scan-modes to record images of the virtual source: "Piezo Table" scan where one and two-dimensional scans were performed by moving a piezo table with a maximum scanning range of 80 × 80 μm^2 in 0.5 μm steps for the one-dimensional line scans and 1 μm for the two-

dimensional area scans. The scanning apertures were either a 25 ± 2 μm slit aperture or a 10 ± 1 μm diameter pinhole aperture (both National Aperture Inc.).

The other scanning mode, "Detector Arm" scan, left the slit/pinhole aperture in a fixed position on the piezo table but moved the whole piezo table and detector setup on a circular guidance rail with center of rotation at the zone plate position. The step size for this scanning process was 0.001°, corresponding to a step size of 6.6 μm. The advantage of the Detector Arm scan is that the scan range was not limited to the 80 μm of the piezo table, making it possible to scan the whole virtual source image for all stagnation pressures p_o.

The helium atoms passing through the slit/pinhole aperture were detected with an electron bombardment ionization detector.[53]

4. MEASUREMENT RESULTS AND ANALYSIS

We have previously discussed the imagining properties of ZPs[35] but give a short summary here for completeness.
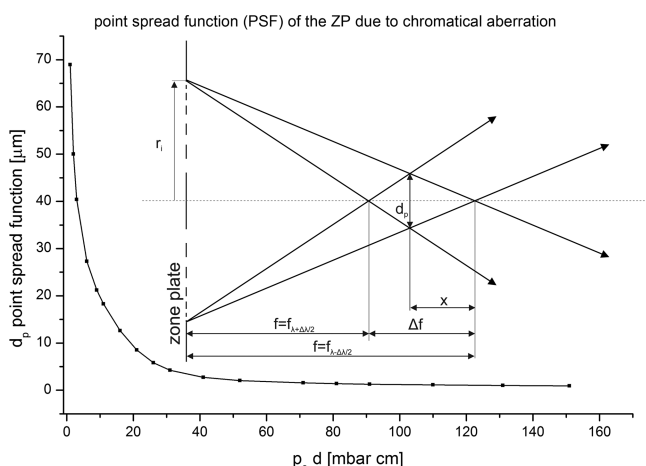
Figure 3. PSF of the Fresnel ZP plotted as a function of stagnation pressure p_o multiplied with the nozzle diameter d_N. The FWHM of the PSF (d_p) decreases with increasing stagnation pressure as the velocity spread of the beam narrows and hence the chromatic aberration decreases.

First, the measured scan function F needs to be corrected for the error introduced by scanning with a slit or pinhole aperture of finite size. F originates from a convolution of the scanned image function of the virtual source G and the transmission function P of the slit and pinhole aperture respectively.

$$F = G*P \tag{2}$$

G can be approximated well with a single Gaussian with a full-width at half-maximum (FWHM) d_s denoting the width of the scanned virtual source size. Thus, d_s can be obtained from a deconvolution of the measured image function F and the slit/pinhole transmission function P.

The second important factor that has to be taken into account when determining the true size of a ZP image is the chromatic point spread function (PSF),[56] which will cause a broadening of the image due to the velocity spread in the beam. The transversal width d_p of the chromatic PSF of a Fresnel ZP is given as[58]

$$d_p = \frac{r_i}{\frac{\lambda}{\Delta\lambda}} \simeq 2\sqrt{\ln(2)}\,\frac{r_i}{S} \tag{3}$$
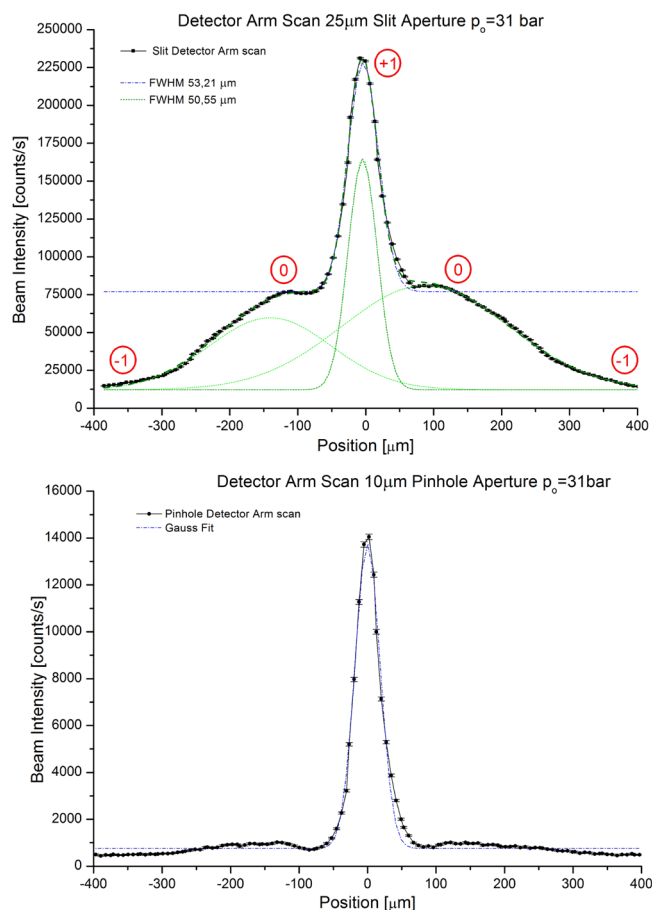
Figure 4. Detector Arm scans for a stagnation pressure of p_o = 31 bar recorded with the 25 μm slit aperture (top) and the 10 μm pinhole aperture (bottom) respectively. The pinhole aperture scan is well fitted with a single Gaussian, depicted as blue-dash-dotted line. For the slit scan, the 0 and −1 order contribution is much larger and has to be fitted separately: green-dashed lines. The two smaller Gaussians on the left and the right side of the middle peak correspond to the two 0 order shares of the imaged beam profile (see Figure 2). The middle peak corresponds to the +1 order focus.

where r_i is the radius of the ZP, λ is the average beam wavelength, and $\Delta\lambda$ is the FWHM of the beam wavelength distribution. The inset in Figure 3 shows the procedure to analytically calculate the PSF by considering two pairs of rays corresponding to different wavelengths ($\lambda \pm \Delta\lambda/2$) that are focused on two different positions whose difference is the width of the PSF. The speed ratio S is a measure for the velocity spread of the beam (see ref 58). In principle, S can be determined experimentally using a TOF measurement. A standard deconvolution procedure for TOF measurements is described in the literature.[3,54] We previously showed that this standard procedure cannot be performed with sufficient accuracy for measurements at high source stagnation pressures p_o, where the velocity distribution is very narrow.[35] Therefore, we chose to use theoretically determined S values calculated using the model described in Section 2 that has shown to describe the parallel velocity distribution accurately.[47] Calculated values of d_p are shown in Figure 3. Note that in Figure 3 as well as in Figure 7 the x-axis corresponds to $p_o d$ in mbar cm. This notation was chosen to stay consistent with previously published results in literature. A pleasant side-effect of the 10 μm diameter nozzle used in our experiment is that the
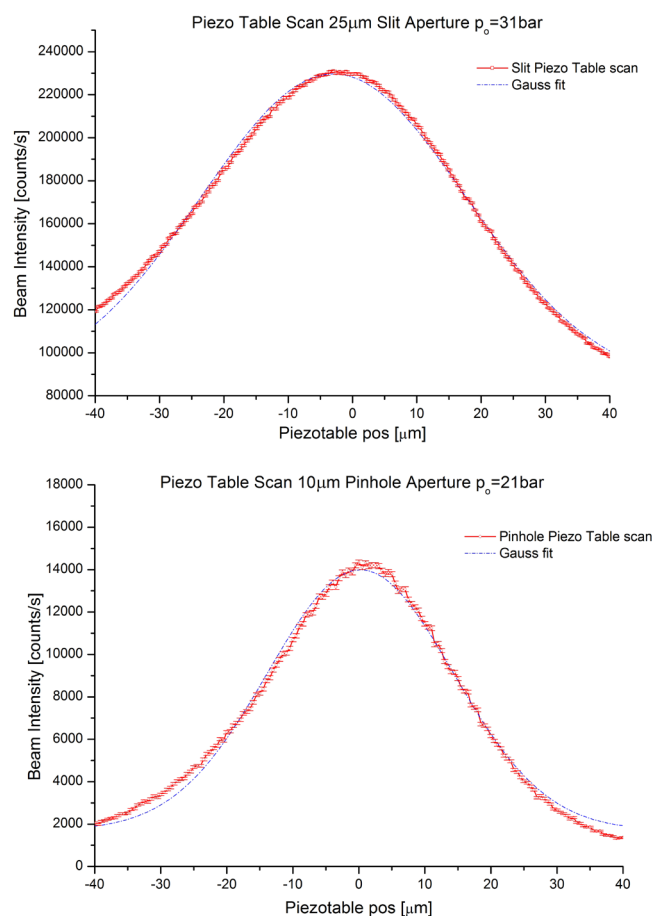
Figure 5. Piezo Table scans for $p_o = 31$ bar with the 25 μm slit aperture (top) and $p_o = 21$ bar with the 10 μm pinhole aperture (bottom) respectively. Gaussian fits are depicted as blue-dashed line. The scan range is so small that the 0 and −1 order essentially only contribute as a constant background that has been subtracted (see Figure 4).

Figure 6. Top: Piezo Table and Detector Arm scan recorded with the 25 μm slit aperture at a beam stagnation pressure of $p_o = 31$ bar. Bottom: Piezo Table and Detector Arm scan recorded with a 10 μm pinhole aperture at a beam stagnation pressure of $p_o = 21$ bar. No normalization has been performed. The agreement is excellent.

numerical values for p_od (in mbar cm) are the same as for p_o. Because the nozzle diameter was kept constant throughout all our experiments but the stagnation pressure was varied, the main text refers to changes in the stagnation pressure p_o.
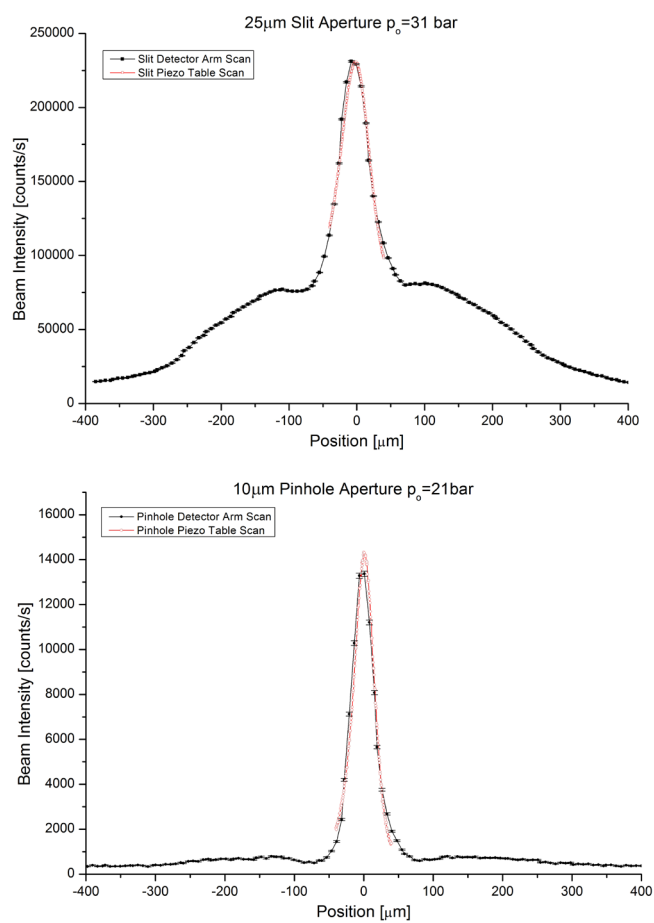
The virtual source of a free jet expansion as well as the PSF can be well approximated with Gaussian functions, hence the PSF contribution can be removed by a deconvolution. Thus, the scanned virtual source size d_s can be expressed as
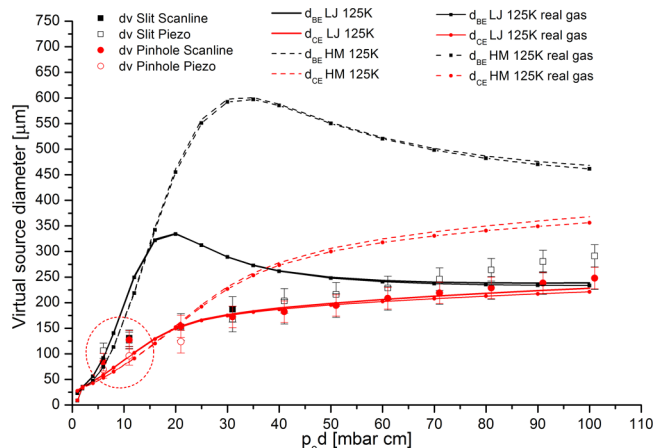
$$d_s = \sqrt{(d_p)^2 + (d_v M)^2} \tag{4}$$

where d_v is the real virtual source size and M is the demagnification factor. For stagnation pressures below $p_o = 17$ bar, the PSF values are approaching the size of the virtual source and a clear distinction between the widening due to the chromatic aberration of the ZP (PSF values) and the real size of the virtual source cannot be made. We therefore decided to present the $p_o < 17$ bar measurements as upper limit values which are not corrected for the PSF. All other measurement results are corrected for the PSF contribution.

The true virtual source size d_v can be derived from the scanned virtual source size d_s by rearranging eq 4

$$d_v = \frac{\sqrt{d_s^2 - d_p^2}}{M} \tag{5}$$

Figure 7. Comparison of the experimentally determined virtual source diameters d_v with the results from the simulations. d_{BE} LJ and d_{BE} HM are the simulated virtual source diameters with the Boltzmann equation and the LJ and the HM potential, respectively. d_{CE} LJ and d_{CE} HM are the simulated virtual source diameters with the continuum expansion model for the LJ and the HM potential, respectively. In addition, a real gas correction is applied. Note that the data for stagnation pressures below 20 bar (circled points) are shown without a d_p correction. This is discussed in Section 4.
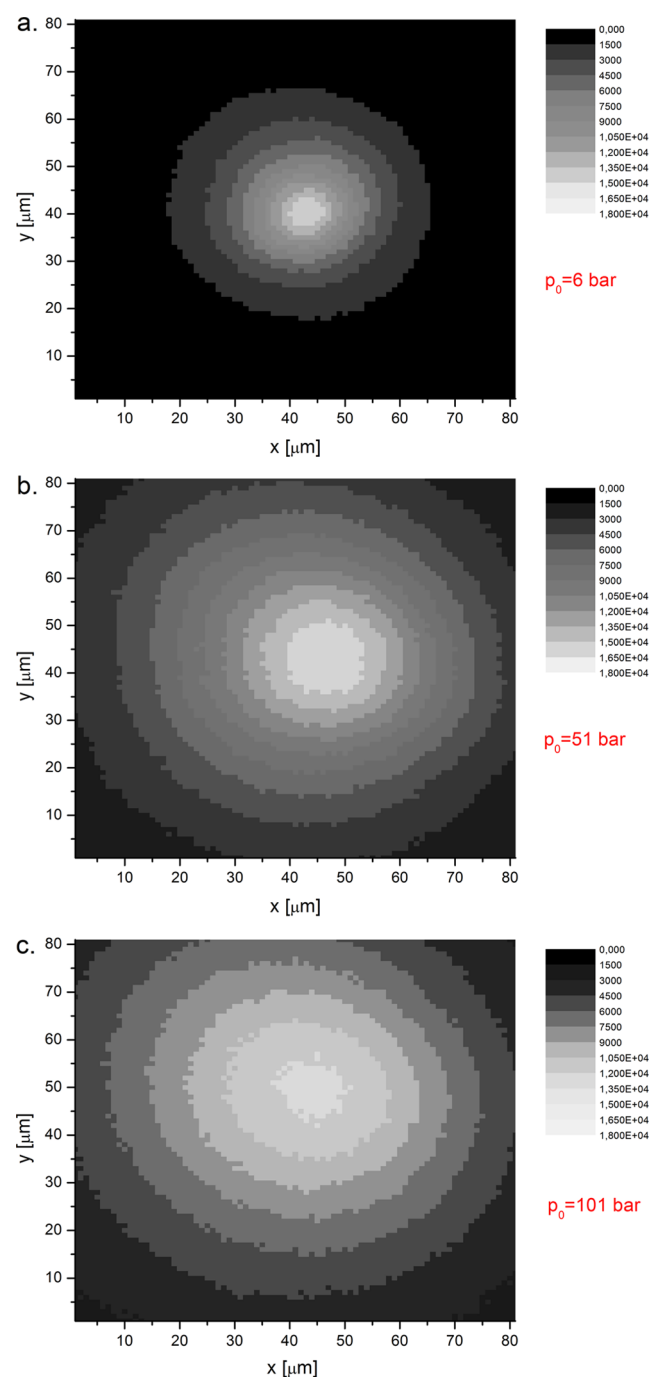
Figure 8. The two-dimensional images of the virtual source for different stagnation pressures p_o. The images are recorded using a ZP as an imaging element and stepping a 10 μm pinhole aperture, located in the image plane of the ZP, in the x/y direction. The scanning process is performed by a piezo table with a step size of 1 μm and a recording time of 1.2 s/step. Note: These measurement results are not corrected, neither for the chromatic aberration of the ZP, nor for the finite size of the scanning aperture. The small image distortions from a radially symmetrical shape can be attributed to temperature fluctuations during the recording process, which lasted around 2 h for each image.

Several Piezo Table and Detector Arm scans were performed for varying stagnation pressures p_o. The resulting virtual source diameters d_v depend crucially on an adequate procedure of extracting the values for the measured image size d_m from the experimental data. To illustrate the fitting procedure, examples of typical experimental data sets with fits are presented in Figures 4 (Detector Arm scans) and 5 (Piezo Table scans). Figure 6 illustrates the excellent agreement between the two scan types.

Figure 4 shows Detector Arm scans performed with the 25 μm slit aperture and the 10 μm pinhole aperture respectively. For the slit scan, the background contribution is much higher. To determine the influence of this strong background signal on the resulting d_v values, we investigated two different fitting strategies for the measurement curve. In one case, we performed a single Gaussian fit with the offset value (background) located at the minimum signal within the central stop region. In the other case, we treated the detected signal as a sum of three intensity distributions of Gaussian shape, corresponding to two 0 order contributions (the central stop in the zone plate splits the 0 order in the scan profile in two parts) and one +1 order contribution, see Figure 2. The different peak height (intensity) and width of the left and right 0 order contribution can be attributed to a not ideal shape of the ZP. An ideal ZP should be symmetric around the center but over/under etching during fabrication can cause the real ZP to give a slightly asymmetric pattern.

The virtual source diameter values originating from the two different fitting strategies lead to variations smaller than the experimental error. For the final comparison between our experimental data and the values of the theoretical model (see Figure 7) the more complex fitting procedure utilizing the three Gaussians was used.

Figure 5 shows Piezo Table scans. The top graph shows a Piezo Table scan performed with the 25 μm slit aperture at $p_o = 31$ bar and the bottom graph represents a Piezo Table pinhole aperture scan recorded at a stagnation pressure of $p_o = 21$ bar. Both data sets are fitted with a single Gaussian, because the Piezo Table scan range is not large enough to enable a good, separate fitting of the background contribution.

The agreement between the two types of scans is excellent. This is illustrated in Figure 6 where Piezo Table and Detector Arm scans are plotted superimposed on each other. Note: No normalization has been performed.

A comparison of the experimentally determined virtual source diameters and the results from the theoretical calculations are shown in Figure 7. As mentioned in Section 2, we use two approaches (BE and continuum expansion (CE) model) with two analytical potentials (LJ and HM). In addition, real gas properties of helium are included for the first time. Theoretical curves calculated by means of the BE are above the curve obtained by means of the CE model and the virtual source diameters estimated by using $T_{\ddagger}^*$ show a nonmonotonic behavior with a maximum value at about 20 and 30 bar for LJ and HM, respectively. By a further increasing of the pressure the curves related to the BE decrease and tend to those estimated by means of the CE model. Above 15 bar, the curves related to the HM potential are above the corresponding ones of the LJ potential. The real gas correction, which modifies the enthalpy of the gas, has only a very limited effect in the measured range, the difference with noncorrected curves also at high pressure is less than the experimental error bars. The best agreement with the data is obtained with the CE model based on the LJ potential, albeit with a small deviation with increasing stagnation pressure. This is consistent with our previous results using a beam at 320 K.[45] On the other hand, in the same previous study the results by De Ponte et al.,[44]

obtained at 77 K by a direct transverse scan on the beam without focusing, were analyzed and the results of calculations based on the HM potential gave a better agreement with respect to those of the LJ one. The investigation of the parallel velocity distribution,[49] which depends on the parallel temperature $T_{\parallel}$, showed also best agreement with the LJ potential for source temperatures above ∼40 K while at lower temperatures the best agreement was obtained with the HM potential. In this study, also the Tang−Toennies−Yiu potential[59] was considered with results very similar to the HM potential. While at low temperature it is not surprising that more refined potentials provide a better fit with the experiment, the results at higher temperatures seem to be in contradiction with the fact that the LJ potential at short-range presents too much repulsion while its attraction is too strong at long-range.[49,60] This is an open problem and we can speculate that at low temperature the discrepancy on the attraction part of the LJ potential causes the failure for fitting the data whereas at higher temperatures the two discrepancies cancel out providing a fortuitous agreement. On the other hand, this agreement is not perfect and, for instance, by increasing the pressure the experimental points shift from the LJ curve and around 100 bar they lie in between the LJ and HM curves of the CE model. Moreover, their trend shows a slope that is more similar to that of the HM curve than the LJ curve. This shift from the LJ curve might be due to an increasing of the background gas between nozzle and skimmer and/or due to the discrepancies in the LJ potential. Because the measurements were performed limiting the maximum pressure to 100 bar in order to reduce the influence of background gas, we can assume that this shift is not completely due to the background, therefore a possible way to gain further information on the problem is performing calculations based on another potential that can provide better agreement. A possible candidate for future investigation is a modified LJ potential[61] that has been employed to explain results of scattering experiments between rare gas systems[60] and to simulate a seeded beam of Ar in He.[62] In fact, the results obtained by this modified LJ potential improved the agreement obtained by those based on LJ and the same may happen also for the gas expansion. Another remark is about the agreement between data and the virtual source diameter estimated by the temperature scaling provided by the CE model. In our model, the estimated diameter depends on the distance of the quitting surface and a suitable temperature $T^{*}_{\ddagger}$. The method of moments provides both quantities but due to the disagreement with the data, its assumptions might be wrong. The spherical symmetry and the dependence only on the distance from the source seem to be reasonable assumptions since the study is performed in a small angular range around the central streamline of the beam. Some doubts can be raised by the assumption of a Gaussian distribution for the velocity because this is an equilibrium distribution while during the expansion the gas is far from equilibrium conditions although a local equilibrium can be assumed. The agreement of the model to predict the parallel velocity distribution[47,49] points out that the problem is likely associated with the perpendicular distribution that should be modified. On the other hand, the calculations show that for higher pressures the BE values tend to those of the CE model, hence the perpendicular distribution has to be only modified for lower pressures. Another possibility is related to the quitting surface that is sharp in the model while it is actually a region of some thickness. In the calculations, $T^{*}_{\ddagger}$ is a decreasing function with increasing the distance from the

nozzle while the value of $T_{\parallel}$ is essentially constant near and beyond the sharp quitting surface. Equation 1 depends on the product of D_{QS} and the square root of $T^{*}_{\ddagger}$ but the correlation between the two quantities might provide a better agreement changing the distance around the estimated D_{QS} while affecting $T_{\parallel}$ in a negligible way. Moreover, especially in the case of a better agreement with the modified LJ potential mentioned above, it would be possible to estimate the thickness of the quitting surface as a difference between D_{QS} and the new estimated value. In any case, from an experimental point of view, the present model provides a reliable estimate of the virtual source size that is useful for the design of experiments where the lateral coherence is an important parameter, such as atom microscopy.

Finally we present the first two-dimensional (2D) images of the virtual source in a supersonic molecular beam. The images were recorded for several stagnation pressure values, using an x/y Piezo Table scan with the 10 μm pinhole aperture. Grayscale images for stagnation pressure values p_o of 6, 51, and 101 bar are presented in Figure 8. For the images recorded at 51 and 101 bar it is obvious that the scanning range of 80 × 80 μm^2 is not sufficient to image the full virtual source. However, the images show nicely the increase of the virtual source diameter with rising stagnation pressures. The small image deviation from a radially symmetrical shape can be attributed to temperature fluctuations during the recording process which lasted around 2 h for each scan.

5. CONCLUSION

We present measurements of the virtual source for a supersonic helium beam, obtained for varying stagnation pressures and a beam temperature of around 125 K. The virtual source diameter varies from 140 ± 30 μm at p_o = 21 bar to 270 ± 25 μm at p_o = 101 bar. The measurements include the first two-dimensional images of a supersonic molecular beam expansions. We compare our results to a theoretical model, which we previously developed to describe experimental data obtained at 320 K.[45] The best description of the experimental data is obtained with a continuum expansion model combined with a Lennard-Jones potential. This findings were also reflected in the study of the He beam at 320 K.[45] A critical discussion of the agreement with the calculations based on the Lennard-Jones potential has shown possible perspective work to be done to further improve the theoretical model. However, the very good agreement between the present model and experimental data over a large temperature range allows us now to perform a series of calculations for optimizing the beam conditions to obtain the highest flux in the central part of the virtual source. This is important, among other applications, for future helium microscopy experiments, where the beam intensity is a crucial issue and where microskimmers with a diameter much smaller than the virtual source are applied.

■ AUTHOR INFORMATION

Corresponding Author
*E-mail: sabrina.eder@uib.no.

Notes
The authors declare no competing financial interest.

■ ACKNOWLEDGMENTS

Michelsen Center for industrial measurement science and technology (MIMT) in Bergen, as well as by the EU project HadronPhysics3- WP20:FutureJet. The Fresnel zone plates were fabricated at the institute for X-ray physics, University of Göttingen, by Stefan Rehbein and Günter Schmahl.

■ REFERENCES

(1) Scoles, G. In *Atomic and Molecular Beam Methodes*; Scoles, G., Ed.; Oxford University Press: New York, 1988; Vols. *1 and 2*.

(2) Pauly, H. In *Atom, Molecule, and Cluster Beams 1*; Pauly, H., Ed.; Springer: Berlin, 2000; Vol. *1*.

(3) Pauly, H. In *Atom, Molecule, and Cluster Beams 2*; Pauly, H., Ed.; Springer: Berlin, 2000; Vol. *2*.

(4) Camparque, R. In *Atomic and Molecular Beams*; Campargue, R., Ed.; Springer: Berlin, 2001.

(5) Täschner, A.; Köhler, E.; Ortjohann, H.-W.; Khoukaz, A. *Nucl. Instrum. Methods Phys. Res., Sect. A* **2011**, *660*, 22−30.

(6) Lehmann, K. K.; Scoles, G. The Ultimate Spectroscopic Matrix. *Science* **1998**, *279*, 2065−2066.

(7) Toennies, J. P.; Vilesov, A. F. Superfluid Helium Droplets: A Uniquely Cold Nanomatrix for Molecules and Molecular Complexes. *Angew. Chem., Int. Ed.* **2004**, *43*, 2622−2648.

(8) Reisinger, T.; Patel, A. A.; Reingruber, H.; Fladischer, K.; Ernst, W. E.; Bracco, G.; Smith, H. I.; Holst, B. Poisson's Spot with Molecules. *Phys. Rev. A* **2009**, *79*, 053823.

(9) Reisinger, T.; Bracco, G.; Holst, B. Particle-Wave Discrimination in Poisson Spot Experiments. *New J. Phys.* **2011**, *13*, 065016.

(10) Arndt, M.; Nairz, O.; Vos-Andreae, J.; Keller, C.; van der Zouw, G.; Zeilinger, A. Wave-Particle Duality of C60 Molecules. *Nature* **1999**, *401*, 680−682.

(11) Arndt, M.; Ekers, A.; von Klitzing, W.; Ulbricht, H. Focus on Modern Frontiers of Matter Wave Optics and Interferometry. *New J. Phys.* **2012**, *14*, 125006.

(12) Cronin, A. D.; Schmiedmayer, J.; Pritchard, D. E. Optics and Interferometry with Atoms and Molecules. *Rev. Mod. Phys.* **2009**, *81*, 1051−1129.

(13) Farías, D.; Rieder, K.-H. Atomic Beam Diffraction from Solid Surfaces. *Rep. Prog. Phys.* **1998**, *61*, 1575.

(14) Bracco, G.; Bruschi, L.; Tatarek, R.; Franchini, A.; Bortolani, V.; Santoro, G. Anomalous Linewidth Behaviour of the S 3 Surface Resonance on Ag(110). *EPL* **1996**, *34*, 687.

(15) Ellis, J.; Graham, A. P.; Hofmann, F.; Toennies, J. P. Coverage Dependence of the Microscopic Diffusion of Na Atoms on the Cu(001) Surface: A Combined Helium Atom Scattering Experiment and Molecular Dynamics Study. *Phys. Rev. B* **2001**, *63*, 195408.

(16) Pedemonte, L.; Tatarek, R.; Vladiskovic, M.; Bracco, G. Anisotropic Self-Diffusion on Ag(110). *Surf. Sci.* **2002**, *507−510*, 129−134.

(17) Jardine, A.; Hedgeland, H.; Alexandrowicz, G.; Allison, W.; Ellis, J. Helium-3 Spin-Echo: Principles and Application to Dynamics at Surfaces. *Prog. Surf. Sci.* **2009**, *84*, 323−379.

(18) Bracco, G.; Holst, B. In *Surface Science Techniques*; Bracco, G., Holst, B., Eds.; Springer Series in Surface Sciences; Springer: New York, 2013; Chapter 12, pp 333−367.

(19) Steurer, W.; Apfolter, A.; Koch, M.; Sarlat, T.; Søndergård, E.; Ernst, W.; Holst, B. The Structure of the Alpha-Quartz (0001) Surface Investigated Using Helium Atom Scattering and Atomic Force Microscopy. *Surf. Sci.* **2007**, *601*, 4407−4411.

(20) Bracco, G.; Tatarek, R.; Vandoni, G. Oxygen Effectiveness in Restructuring the Ag(110) Surface: The p $(3 \times 1)O$ Chemisorbed Phase. *Phys. Rev. B* **1990**, *42*, 1852−1855.

(21) Mete, E.; Demiroglu, I.; Albayrak, E.; Bracco, G.; Ellialtioglu, S.; Danisman, M. Influence of Steps on the Tilting and Adsorption Dynamics of Ordered Pentacene Films on Vicinal Ag(111) Surfaces. *J. Phys. Chem. C* **2012**, *116*, 19429−19433.

(22) Cavanna, D.; Bracco, G.; Renzi, V. D.; Corradini, V.; Biagi, R.; del Pennino, U. Ordered Phases and Temperature Behaviour of CH 3

(23) Bracco, G.; Scoles, G. Study of the Interaction Potential Between He and a Self-Assembled Monolayer of Decanethiol. *J. Chem. Phys.* **2003**, *119*, 6277−6281.

(24) Bracco, G.; Acker, J.; Ward, M. D.; Scoles, G. Helium Diffraction Study of Organic Single-Crystal Surfaces: Hydrogen-Bonded and Methyl-Terminated (001) Cleavage Planes of a Guanidinium Methanesulfonate Crystal. *Langmuir* **2002**, *18*, 5551−5557.

(25) Pedemonte, L.; Bracco, G.; Boragno, C.; Buatier de Mongeot, F.; Valbusa, U. Smoothing of Nanoscale Surface Ripples Studied by He Atom Scattering. *Phys. Rev. B* **2003**, *68*, 115431.

(26) Bracco, G.; Cavanna, D. Decay of Nanoripples on Au(111) Studied by He Atom Scattering. *Phys. Rev. B* **2007**, *76*, 033411.

(27) Steurer, W.; Apfolter, A.; Koch, M.; Ernst, W. E.; Holst, B.; Søndergård, E.; Manson, J. R. Observation of the Boson Peak at the Surface of Vitreous Silica. *Phys. Rev. Lett.* **2007**, *99*, 035503.

(28) Becker, J. S.; Brown, R. D.; Killelea, D. R.; Yuan, H.; Sibener, S. J. Comparative Surface Dynamics of Amorphous and Semicrystalline Polymer Films. *Proc. Natl. Acad. Sci. U.S.A.* **2011**, *108*, 977−982.

(29) Wu, Y.; Toccoli, T.; Koch, N.; Iacob, E.; Pallaoro, A.; Rudolf, P.; Iannotta, S. Controlling the Early Stages of Pentacene Growth by Supersonic Molecular Beam Deposition. *Phys. Rev. Lett.* **2007**, *98*, 076601.

(30) Casalis, L.; Danisman, M. F.; Nickel, B.; Bracco, G.; Toccoli, T.; Iannotta, S.; Scoles, G. Hyperthermal Molecular Beam Deposition of Highly Ordered Organic Thin Films. *Phys. Rev. Lett.* **2003**, *90*, 206101.

(31) Iannotta, S.; Toccoli, T.; Biasioli, F.; Boschetti, A.; Ferrari, M. Highly Ordered Films of Quaterthiophene Grown by Seeded Supersonic Beams. *Appl. Phys. Lett.* **2000**, *76*, 1845−1847.

(32) Patton, F. S.; Deponte, D. P.; Elliott, G. S.; Kevan, S. D. Speckle Patterns with Atomic and Molecular de Broglie Waves. *Phys. Rev. Lett.* **2006**, *97*, 013202.

(33) Koch, M.; Rehbein, S.; Schmahl, G.; Reisinger, T.; Bracco, G.; Ernst, W. E.; Holst, B. Imaging with Neutral Atoms - A New Matter-Wave Microscope. *J. Microsc.* **2008**, *229*, 1−5.

(34) Witham, P. J.; Sanches, E. J. Increased Resolution in Neutral Atom Microscopy. *J. Microsc.* **2012**, *248*, 223−227.

(35) Eder, S. D.; Reisinger, T.; Greve, M. M.; Bracco, G.; Holst, B. Focusing of a Neutral Helium Beam Below One Micron. *New J. Phys.* **2012**, *14*, 073014.

(36) Miller, D. In *Atomic and Molecular Beam Methodes*; Scoles, G., Ed.; Oxford University Press: New York, 1988; Vol. *1*, Chapter 2, pp 14−53.

(37) Kappes, M.; Leutwyler, S. In *Atomic and Molecular Beam Methodes*; Scoles, G., Ed.; Oxford University Press: New York, 1988; Vol. *1*, pp 380−408.

(38) Campargue, R. Progress in Overexpanded Supersonic Jets and Skimmed Molecular Beams in Free-Jet Zones of Silence. *J. Phys. Chem.* **1984**, *88*, 4466−4474.

(39) Morse, M. D. In *Atomic, Molecular, and Optical Physics, Atoms and Molecules*; Dunning, F. B., Hulet, R. G., Eds.; Academic Press, Inc.: New York, 1996; Vol. *29B*, Chapter 2, pp 21−47.

(40) Beijerinck, H.; Verster, N. Absolute Intensities and Perpendicular Temperatures of Supersonic Beams of Polyatomic Gases. *Physica B+C (Amsterdam)* **1981**, *111*, 327−352.

(41) Beijerinck, H.; Kaashoek, G.; Beijers, J.; Verheijen, M. Non-Maxwellian Velocity Distributions in the Transition Region of Supersonic Expansions of the Noble Gases He, Ne and Ar. *Physica B+C (Amsterdam)* **1983**, *121*, 425−436.

(42) Verheijen, M.; Beijerinck, H.; Renes, W.; Verster, N. A Quantitative Description of Skimmer Interaction in Supersonic Secondary Beams: Calibration of Absolute Intensities. *Chem. Phys.* **1984**, *85*, 63−71.

(43) Beijerinck, H.; Gerwen, R. V.; Kerstel, E.; Martens, J.; Vliembergen, E. V.; Smits, M.; Kaashoek, G. Campargue-Type Supersonic Beam Sources: Absolute Intensities, Skimmer Trans-

S Self-Assembled Monolayers on Au(111). *J. Phys.: Condens. Matter* **2007**, *19*, 305019.

mission and Scaling Laws for Mono-Atomic Gases He, Ne and Ar. *Chem. Phys.* **1985**, *96*, 153−173.

(44) DePonte, D. P.; Kevan, S. D.; Patton, F. S. Brightness of Micronozzle Helium Source. *Rev. Sci. Instrum.* **2006**, *77*, 055107.

(45) Reisinger, T.; Bracco, G.; Rehbein, S.; Schmahl, G.; Ernst, W. E.; Holst, B. Direct Images of the Virtual Source in a Supersonic Expansion. *J. Phys. Chem. A* **2007**, *111*, 12620−12628.

(46) Reisinger, T.; Greve, M. M.; Eder, S. D.; Bracco, G.; Holst, B. Brightness and Virtual Source Size of a Supersonic Deuterium Beam. *Phys. Rev. A* **2012**, *86*, 043804.

(47) Pedemonte, L.; Bracco, G.; Tatarek, R. Theoretical and Experimental Study of He Free-Jet Expansions. *Phys. Rev. A* **1999**, *59*, 3084−3087.

(48) Toennies, J. P.; Winkelmann, K. Theoretical Studies of Highly Expanded Free Jets: Influence of Quantum Effects and a Realistic Intermolecular Potential. *J. Chem. Phys.* **1977**, *66*, 3965−3979.

(49) Pedemonte, L.; Bracco, G. Study of He Flow Properties to Test He Dimer Potentials. *J. Chem. Phys.* **2003**, *119*, 1433−1441.

(50) Toennies, J. On the Validity of a Modified Buckingham Potential for the Rare Gas Dimers at Intermediate Distances. *Chem. Phys. Lett.* **1973**, *20*, 238−241.

(51) Hurly, J. J.; Moldover, M. R. Ab Initio Values of the Thermophysical Properties of Helium as Standards. *J. Res. Natl. Inst. Stand. Technol.* **2000**, *105*, 667−688.

(52) McCarty, R. D.;Arp, V. D. In *Advances In Cryogenic Engineering*; Fast, R. W., Ed.; Springer: New York, 1990; Vol. *35*, Chapter part B, pp 1465−1475.

(53) Apfolter, A. Wiederaufbau und Test einer He-Streuapparatur und erste Streuexperimente an amorpher sowie kristalliner SiO2-Oberfläche. M.Sc. Thesis, Graz University of Technology, 2005.

(54) Auerbach, D. J. In *Atomic and Molecular Beam Methodes*; Scoles, G., Ed.; Oxford University Press: New York, 1988; Vol. *1*, pp 362−379.

(55) Rehbein, S. Nanostructuring of Zone Plates for Helium Atom Beam Focusing. *J. Phys. IV* **2003**, *104*, 207−210.

(56) Michette, A. G. In *Optical Systems for Soft X-Rays*; Michette, A., Ed.; Plenum Press: New York, 1968.

(57) Rehbein, S.; Doak, R.; Grisenti, R.; Schmahl, G.; Toennies, J.; Wöll, C. Nanostructuring of Zone Plates for Helium Atom Beam Focusing. *Microelectron. Eng.* **2000**, *53*, 685−688.

(58) Reisinger, T.; Holst, B. Neutral Atom and Molecule Focusing Using a Fresnel Zone Plate. *J. Vac. Sci. Technol., B* **2008**, *26* (6), 2374−2379.

(59) Tang, K. T.; Toennies, J. P.; Yiu, C. L. Accurate Analytical He-He van der Waals Potential Based on Perturbation Theory. *Phys. Rev. Lett.* **1995**, *74* (9), 1546−1549.

(60) Pirani, F.; Brizi, S.; Roncaratti, L. F.; Casavecchia, P.; Cappelletti, D.; Vecchiocattivi, F. Beyond the Lennard-Jones Model: A Simple and Accurate Potential Function Probed by High Resolution Scattering Data Useful for Molecular Dynamics Simulations. *Phys. Chem. Chem. Phys.* **2008**, *10*, 5489−5503.

(61) Pirani, F.; Albertí, M.; Castro, A.; Moix Teixidor, M.; Cappelletti, D. Atom-Bond Pairwise Additive Representation for Intermolecular Potential Energy Surfaces. *Chem. Phys. Lett.* **2004**, *394*, 37−44.

(62) Longo, S.; Diomede, P.; Laricchiuta, A.; Colonna, G.; Capitelli, M.; Ascenzi, D.; Scotoni, M.; Tosi, P.; Pirani, F. *Computational Science and Its Applications - ICCSA 2008*; Gervasi, O., Murgante, B., Laganá, A., Taniar, D., Mun, Y., Gavrilova, M., Eds.; Springer Series Lecture Notes in Computer Science; Springer: Berlin; 2008; Vol. *5072*, pp 1131−1140.

12

dx.doi.org/10.1021/jp4082855 | *J. Phys. Chem. A* 2014, 118, 4−12